

1 **X-Structured  $\alpha$ -FeOOH with Enhanced Charge**  
2 **Separation for Visible-Light-Driven Photocatalytic**  
3 **Overall Water Splitting**

4  
5 Tianqi Wang,<sup>[a]</sup> Zhifeng Jiang<sup>\*[a, b]</sup>, Ka Him Chu,<sup>[a]</sup> Dan Wu,<sup>[a]</sup> Bo Wang,<sup>[a]</sup> Hongli Sun,<sup>[a]</sup>  
6 Ho Yin Yip,<sup>[a]</sup> Taicheng An,<sup>[c]</sup> Huijun Zhao,<sup>[d, e]</sup> and Po Keung Wong<sup>\*[a]</sup>

7  
8 <sup>[a]</sup> School of Life Sciences, The Chinese University of Hong Kong, Shatin, NT, Hong  
9 Kong, China. Email: pkwong@cuhk.edu.hk

10 <sup>[b]</sup> Institute for Energy Research, School of Chemistry and Chemical Engineering,  
11 Jiangsu University, Zhenjiang, Jiangsu 212013, China. Email: ntjiangzf@sina.com

12 <sup>[c]</sup> Institute of Environmental Health and Pollution Control, School of Environmental  
13 Science and Engineering, Guangdong University of Technology, Guangzhou 510006,  
14 Guangdong, China.

15 <sup>[d]</sup> Centre for Clean Environment and Energy, Griffith Scholl of Environment, Griffith  
16 University, Queensland 4222, Australia

17 <sup>[e]</sup> Laboratory of Nanomaterials and Nanostructures, Institute of Solid State Physics,  
18 Chinese Academy of Sciences, Hefei 230031, Anhui, China

Accepted Manuscript

19  
20  
21  
22  
23  
24  
25  
26  
27  
28  
29

30 **Abstract:** Photocatalytic overall water splitting (POWS) is a promising route for  
31 converting solar energy into green and sustainable energy. Herein, we report a  
32 facile hydrothermal approach to fabricate X-structured  $\alpha$ -FeOOH  
33 photocatalysts enclosed with high-index facets for POWS. The X-structured  $\alpha$ -  
34 FeOOH photocatalysts exhibited enhanced visible-light-driven (VLD) POWS  
35 activities in comparison with that of FeOOH without X-structures, with the  
36 maximum  $H_2$  and  $O_2$  evolution rate of  $9.2$  and  $4.7 \mu\text{mol}\cdot\text{h}^{-1}\cdot\text{g}^{-1}$ , respectively. The  
37 morphology and particle size of  $\alpha$ -FeOOH could be controlled by adjusting the  
38  $\text{NH}_4\text{F}$  concentration in the precursors. The photo-depositions of Pt and  $\text{RuO}_2$   
39 revealed the specially separated reduction and oxidation centers on the surface  
40 of X-structured FeOOH, with the oxidation active sites selectively locating on  
41 the edges of FeOOH X-structures. The electrochemical experiments further  
42 affirmed the enhanced charge separation of X-structured FeOOH. The smaller  
43 particle size and unique X-structures of  $\alpha$ -FeOOH photocatalyst were  
44 evidenced to enhance the POWS performance due to the large specific surface  
45 area, high-ratio exposure of  $\{3\bar{1}\bar{1}\}$  facets, high electron transfer efficiency and  
46 effective separation of photo-generated electron-hole pairs. The current study  
47 revealed that the X-structured  $\alpha$ -FeOOH products could serve as cost-effective  
48 and stable photocatalysts for POWS.

## 49 Introduction

50 Driven by the global energy crisis and environmental challenge, increased  
51 attention has been attracted to develop efficient photocatalysts for exploring  
52 clean and sustainable energy. Photocatalytic overall water splitting (POWS) is  
53 considered as one of the most effective ways for energy generation.<sup>[1]</sup> In the  
54 past decades, various kinds of photocatalysts, such as metal oxides and  
55 oxyhydroxides, have been synthesized and utilized for water splitting.<sup>[2]</sup>  
56 Admittedly, numerous photocatalysts exhibited good performance for  $H_2$  or  $O_2$   
57 generation, but most only executed water-splitting half-reactions (i.e. water

58 oxidation or reduction),<sup>[3]</sup> with even fewer photocatalysts able to directly split  
59 water to O<sub>2</sub> and H<sub>2</sub> under visible light (VL) irradiation.<sup>[4]</sup> In addition, to improve  
60 the POWS performance of photocatalysts, the loading of co-catalyst(s) such as  
61 Pt, Au and RuO<sub>2</sub>, etc. was commonly adopted to lower the activation  
62 energy/overpotential and/or assist the electron-hole separation.<sup>[5]</sup> However, the  
63 adoption of co-catalyst(s) significantly increases the cost and thus hinders their  
64 large-scale application to some extent. Therefore, a cost-effective and VL  
65 induced photocatalytic system for POWS without using co-catalyst is urgently  
66 pursued to meet the needs of terawatt solar energy transfer.

67 One of the earth-abundant catalysts, iron oxyhydroxides (e.g.  $\alpha$ -,  $\beta$ -,  $\gamma$ - and  
68  $\delta$ -FeOOH), on the other hand, are good alternatives for water splitting under VL  
69 because of their narrow band gap, high stability and ample availability.<sup>[6]</sup> For  
70 instance, Seabold and Choi reported a BiVO<sub>4</sub> coated FeOOH photocatalyst with  
71 enhanced water oxidation performance.<sup>[7]</sup> Kim *et al.* reported a FeOOH/Fe<sub>2</sub>O<sub>3</sub>  
72 thin film for efficient solar water splitting.<sup>[8]</sup> In addition, bare  $\delta$ -FeOOH and  
73 Ni(OH)<sub>2</sub> loaded  $\delta$ -FeOOH were used as promising photocatalysts for H<sub>2</sub>  
74 production.<sup>[6d, 9]</sup> Nevertheless, to the best of our knowledge, the direct splitting  
75 of pure water into H<sub>2</sub> and O<sub>2</sub> by bare  $\alpha$ -FeOOH has not been studied, and thus  
76 the feasibility of POWS over  $\alpha$ -FeOOH is unknown.

77 The photocatalytic efficiency of micro-/nano-semiconductors is closely  
78 interrelated with their shape, size and exposed facets.<sup>[10]</sup> For instance, the  
79 degradation rate of rhodamine B by FeOOH nanorods was more than two times  
80 faster than that of FeOOH microrods.<sup>[11]</sup>  $\alpha$ -FeOOH particles with various  
81 morphologies (e.g. rod-like, array-like, and pancake-like morphology) exhibited  
82 different photocatalytic efficiencies toward the acetaldehyde decomposition,  
83 which was due to the differences in their shapes and specific surface areas.<sup>[12]</sup>  
84 In addition, it has been widely reported that the high-index facets will promote  
85 the photocatalytic performance of semiconductors due to the high density of  
86 atomic steps, ledges and kinks, which usually serve as active sites for surface  
87 catalytic reactions.<sup>[13]</sup> However, the high-index facets usually disappear during

88 the crystal growth process to minimize the total surface energy, which makes it  
89 difficult to fabricate photocatalyst with exposure of high-index facets.<sup>[14]</sup> Thus, it  
90 is interesting to design and synthesize the high-index faceted photocatalysts to  
91 promote the efficiency of POWS.

92 Herein, we reported a facile way to fabricate a unique X-structured  $\alpha$ -  
93 FeOOH photocatalyst enclosed by 16 high-index  $\{3\bar{1}\bar{1}\}$  facets. The POWS  
94 performance and photo-stability of the as-prepared  $\alpha$ -FeOOH photocatalysts  
95 were investigated under VL irradiation. The morphology, facet and size effects  
96 toward the POWS activity were also examined. The work presented here can  
97 provide a simple yet effective approach to prepare  $\alpha$ -FeOOH based  
98 photocatalysts for POWS.

## 99 Results and Discussion

100 As shown in the XRD pattern of FeOOH-30F (Figure 1a), all the diffraction  
101 peaks were indexed to  $\alpha$ -FeOOH (PDF card No.: 99-0055), revealing that  $\alpha$ -  
102 FeOOH was successfully prepared with pure phase. The unique X-like structure  
103 of FeOOH-30F was clearly observed in the TEM image (Figure 1b), with the  
104 angle between two branches of  $\sim 117^\circ$ . As it could be seen in Figure 1c-1f, all  
105 the selected-area electron diffraction (SAED) patterns obtained from different  
106 positions labeled in Figure 1b revealed an angle of  $58.9^\circ$  between the (130) and  
107 (112) planes of  $\alpha$ -FeOOH, which was identical to the theoretical angle between  
108 (130) and (112) planes. The corresponding lattice fringes of  $\sim 0.26$  and  $\sim 0.15$   
109 nm in the HRTEM images matched well with the interplanar spacings of (130)  
110 and (112) planes of  $\alpha$ -FeOOH, respectively. The predominantly exposed facets  
111 of the X-structured  $\alpha$ -FeOOH crystals could be calculated to be high-index  $\{3\bar{1}\bar{1}\}$   
112  $\bar{1}\}$  facets according to the crystallographic structure of  $\alpha$ -FeOOH. Therefore, it  
113 could be induced that the X-structured  $\alpha$ -FeOOH crystal was enclosed with 16  
114 high-index  $\{3\bar{1}\bar{1}\}$  facets. Based on the previous study,<sup>[15]</sup> the X-structured  $\alpha$ -  
115 FeOOH with multiple high-index  $\{3\bar{1}\bar{1}\}$  facets may serve as an efficient  
116 photocatalyst for POWS.

117 To better understand the formation mechanism of X-structured  $\alpha$ -FeOOH,  
118 some conditional experiments were carried out. As demonstrated in the FESEM  
119 images (Figure 2 and Figure S1),  $\text{NH}_4\text{F}$  was noted to play an important role in  
120 controlling the morphology of products. In the absence of  $\text{NH}_4\text{F}$  (Figure S1d),  
121 the product was composed of numerous nanospheres with the diameter of ca.  
122 50 nm. With the initial  $\text{NH}_4\text{F}$  concentration of 30, 60 and 120 mM, the resultant  
123 products displayed uniform X-shaped structures with smooth surfaces, and  
124 their particle sizes increased with the increasing  $\text{NH}_4\text{F}$  concentration (Figure  
125 2a-2c). However, when the  $\text{NH}_4\text{F}$  concentration further increased to 180 mM,  
126 some microrods and nanospheres were observed (Figure 2d). The results  
127 revealed that the X-structured  $\alpha$ -FeOOH could be produced only at suitable  
128  $\text{NH}_4\text{F}$  concentrations. Details for the relationship of the particle size of X-  
129 structured crystals and the  $\text{NH}_4\text{F}$  dosage were listed in Table 1. In addition, the  
130 hydrothermal temperature for the preparation of X-structured  $\alpha$ -FeOOH was  
131 optimized. As shown in Figure S2, the X-shaped structures with some irregular  
132 particles were initially formed with the hydrothermal temperature as low as 100  
133  $^\circ\text{C}$ . The sample prepared at 120  $^\circ\text{C}$  (Figure S2c) displayed uniform X-shaped  
134 structures. No noticeable changes in the morphology were observed when the  
135 reaction temperature increased to 140  $^\circ\text{C}$  (Figure S2d). Thus, the optimized  
136 hydrothermal temperature for the fabrication of X-structured  $\alpha$ -FeOOH was 120  
137  $^\circ\text{C}$ . Moreover, the phase composition of the products was also dependent on  
138 the utilization of chemicals. As it could be observed in the FESEM images  
139 (Figure S1) and the XRD patterns (Figure S3),  $\text{Fe}_2\text{O}_3$  nanospheres were  
140 obtained in the absence of  $\text{NH}_4\text{F}$ ,  $\beta$ -FeOOH (akaganeite) was obtained with  
141 irregular shapes in the absence of  $\text{Fe}^{2+}$  or urea, while hexagonal  $\text{Fe}_3\text{O}_4$  disks  
142 with strong magnetic property and FeOOH microrods were obtained without the  
143 addition of  $\text{Fe}^{3+}$ . Thus, all the four chemicals (i.e.  $\text{FeCl}_2$ ,  $\text{FeCl}_3$ ,  $\text{NH}_4\text{F}$  and urea)  
144 were essential for the formation of pure  $\alpha$ -FeOOH with uniform X-shaped  
145 structures. To understand the ion ( $\text{NH}_4^+$  and  $\text{F}^-$ ) effect on the formation of X-  
146 shaped morphology,  $\text{NH}_4\text{Cl}$  or  $\text{NaF}$  was used instead of  $\text{NH}_4\text{F}$ . As illustrated in

147 the FESEM images (Figure S1e and S1f), X-shaped morphology was observed  
148 in the product treated with NaF, while the morphology of the product treated  
149 with NH<sub>4</sub>Cl was similar as that synthesized in the absence of NH<sub>4</sub>F. This  
150 suggested that it was F<sup>-</sup> rather than NH<sub>4</sub><sup>+</sup> ions that resulted in the unique X-  
151 shaped morphology of α-FeOOH. The potential role of F<sup>-</sup> ions on the formation  
152 of X-shaped α-FeOOH is that F<sup>-</sup> ions will preferentially adsorb on the (010) faces  
153 of α-FeOOH crystals during the crystallization growth process, thus the  
154 crystallization growth rate at [010] direction is inhibited, leading to the formation  
155 of four branches.<sup>[16]</sup>

156 From the XRD results (Figure 3), for FeOOH-30F, FeOOH-60F and FeOOH-  
157 120F samples, all the diffraction peaks were indexed to α-FeOOH (PDF card  
158 No.: 99-0055, marked with \*), and no impurity related peaks were observed.  
159 However, for the FeOOH-180F sample, some β-FeOOH peaks were found in  
160 the XRD pattern (Figure 3, marked with #), indicating that high NH<sub>4</sub>F  
161 concentration would lead to the formation of β-FeOOH. As for the FeOOH  
162 without X-structures, its FESEM image (Figure S4a) revealed a hierarchically  
163 plate-like morphology, with the average particle size around 0.32 μm and the  
164 thickness around 0.04 μm. According to the XRD pattern (Figure S4b), the as-  
165 synthesized plate-like sample was indexed to pure α-FeOOH.

166 The UV-vis DRS of the X-structured FeOOH products were shown in Figure  
167 4a. The four FeOOH samples almost shared the same feature of light  
168 absorption. All the absorption edges were centered at the visible light region  
169 around 600 nm. The FeOOH-30F exhibited the highest light adsorption capacity  
170 in almost all the wavelength ranges, indicating a relatively stronger light capture  
171 ability. The band gap energy ( $E_g$ ) of semiconductors can be estimated by using  
172 the Kubelka–Munk function  $ah\nu = A(h\nu - E_g)^{n/2}$ , where  $\alpha$  is the absorption  
173 coefficient,  $h\nu$  is the photo energy, and  $n = 1$  for α-FeOOH as a direct  
174 semiconductor.<sup>[17]</sup> As shown in the plots of transformed Kubelka–Munk function  
175 versus light energy (Figure 4a, inset), the  $E_g$  values of FeOOH-30F, FeOOH-  
176 60F, FeOOH-120F and FeOOH-180F samples were examined to be 2.06, 2.12,

177 2.10 and 2.00 eV, respectively, which were consistent with the previous  
178 studies.<sup>[11, 18]</sup> To better understand the band structure of X-structured FeOOH,  
179 taking FeOOH-30 as an example, the position of valence band maximum (VBM)  
180 was estimated by the valence band XPS spectrum (Figure 4b). The result  
181 showed that the VBM of FeOOH-30F was +1.68 eV (vs. NHE). By the equation  
182  $E_{CB} = E_{VB} - E_g$  ( $E_{CB}$  is conduction band minimum (CBM) potential and  $E_{VB}$  is VBM  
183 potential),<sup>[19]</sup> the CBM of FeOOH-30F was calculated to be -0.38 eV (vs. NHE).  
184 This value was consistent with that examined by Mott-Schottky plot (Figure 4c).  
185 Based on the results, a diagram of the band structure of FeOOH-30F was  
186 demonstrated in Figure 4d.

187 The elemental composition and valence state of the as-prepared  $\alpha$ -FeOOH  
188 photocatalyst were characterized by XPS (Figure 5). In the XPS spectra of Fe  
189 2p of FeOOH-30F (Figure 5a), two major peaks of Fe (III) together with two  
190 shake-up satellites were observed at 711.3 (Fe 2p<sub>3/2</sub>), 725.0 (Fe 2p<sub>1/2</sub>), 719.8  
191 (Fe 2p<sub>3/2</sub> sat.) and 733.9 (Fe 2p<sub>1/2</sub> sat.) eV, respectively, indicating that the  
192 chemical state of Fe in X-structured  $\alpha$ -FeOOH was 3+.<sup>[20]</sup> In the region of O 1s  
193 in XPS spectrum (Figure 5b), there were two strong peaks, which could be  
194 deconvoluted into three peaks located at 529.7, 531.0 and 532.3 eV. They were  
195 attributed to absorbed water, Fe-O-Fe bond, Fe-O-H bond and H-O-H bond,  
196 respectively.<sup>[21]</sup>

197 The POWS performance of X-structured  $\alpha$ -FeOOH samples was  
198 investigated under visible light irradiation without any sacrificial agent and co-  
199 catalyst. Figure 6a showed a typical time course of POWS over FeOOH-30F.  
200 Nearly stoichiometric evolution of hydrogen and oxygen was observed within  
201 12 h, with the molar ratio of H<sub>2</sub> to O<sub>2</sub> around two, indicating that overall water  
202 splitting did occur. As demonstrated in Figure 6b, FeOOH-30F showed the  
203 highest H<sub>2</sub> and O<sub>2</sub> evolution rates of 9.2 and 4.7  $\mu\text{mol}\cdot\text{h}^{-1}\text{g}^{-1}$ , respectively. For  
204 the FeOOH-60F, FeOOH-120F and FeOOH-180F samples, the generated  
205 amounts of H<sub>2</sub>/O<sub>2</sub> were 6.1/3.2, 5.4/2.7 and 1.9/1.0  $\mu\text{mol}\cdot\text{h}^{-1}\text{g}^{-1}$ , respectively.  
206 Considering the photocatalytic performance, the X-structured  $\alpha$ -FeOOH

207 photocatalysts prepared in this work were among the high level for visible light  
208 water splitting compared with recently reported work (see details in the  
209 Supporting Information, Table S1). The results also suggested that the  
210 generated gas amounts increased with the decreasing particle size, this was  
211 mainly due to the change of specific surface area. As shown in Figure 7 and  
212 Table 1, the FeOOH-30 sample exhibited the largest specific surface area of  
213  $29.60 \text{ m}^2\text{g}^{-1}$ , followed by the other three FeOOH samples in sequence. The  
214 larger surface area may provide more active sites, which can contribute to the  
215 adsorption of molecules and light harvesting, and thus enhance the  
216 photocatalytic efficiency.<sup>[17a]</sup> Despite the large specific surface area, smaller  
217 particle size normally favors the photo-generated electrons reaching the  
218 surface for better utilization in the photochemical process,<sup>[6c]</sup> which was also  
219 reported by Wang and co-authors.<sup>[22]</sup> Therefore, the small particle size of  $\alpha$ -  
220 FeOOH catalysts was crucial for the photocatalytic activity.

221 As photo-generated electrons have an important influence on the POWS  
222 process, transient photocurrent responses were measured by multiple on-off  
223 light irradiation cycles to understand the photophysical behavior of the photo-  
224 excited charge carriers. As compared in Figure 8, the FeOOH-30F electrode  
225 exhibited the highest photocurrent intensity, followed by FeOOH-60, FeOOH-  
226 120F and FeOOH-180F electrodes. Since the photocurrent density  
227 demonstrates the separation efficiency of photo-generated electron-hole pairs  
228 within electrodes,<sup>[23]</sup> the higher photocurrent density implies a lower electron-  
229 hole pair recombination rate and a higher photo-generated electron transfer  
230 efficiency. The photocurrent experimental results provided another potential  
231 reason for the different POWS efficiencies of X-structured  $\alpha$ -FeOOH  
232 photocatalysts.

233 In particular, to demonstrate the importance of the special X-like structure,  
234 the POWS efficiencies of X-like FeOOH and plate-like FeOOH were compared  
235 (Figure 9). Obviously, the X-structured FeOOH-30F showed a much faster gas  
236 evolution rate than that of plate-like FeOOH. More importantly, for the plate-like

237 FeOOH sample, no H<sub>2</sub> and O<sub>2</sub> were generated after four hours, revealing a  
238 relatively low photocatalytic activity. As shown in Figure 9b, the photocurrent of  
239 X-structured FeOOH was significantly higher than that of plate-like FeOOH,  
240 indicating a higher photo-generated electron transfer efficiency of the X-  
241 structured sample. The low recombination and superior separation of the photo-  
242 generated electron-hole pairs of X-structured FeOOH were also evidenced by  
243 the room-temperature photoluminescence (PL) spectra (Figure 9c), with a  
244 much lower PL intensity compared to that of plate-like FeOOH. In addition, as  
245 demonstrated in the electrochemical impedance spectroscopy (EIS) Nyquist  
246 plots (Figure 9d), the X-structured FeOOH exhibited a much smaller diameter  
247 of the semicircle arc, indicating a faster interfacial charge transfer to the  
248 electron acceptor.<sup>[24]</sup> That is to say, the X-like structures bounded by multiple  
249 high-index facets can facilitate the charge transfer and suppress the  
250 recombination of charge carriers. In addition, it is worth pointing out that  
251 although the plate-like FeOOH exhibited a larger specific surface area (Table 1  
252 and Figure 7), its POWS efficiency is still lower than that of X-structured  
253 FeOOH. This observation suggested that the morphological evolution of X-  
254 structured FeOOH contributes more to the POWS performance than the  
255 specific surface area.

256 To further understand the mechanism of efficient charge separation for X-  
257 structured FeOOH, the photo-depositions of Pt and RuO<sub>2</sub> on X-structured  
258 FeOOH were carried out. The reduction and oxidation active sites of  
259 photocatalysts can be indicated by the distribution of photo-deposited Pt and  
260 RuO<sub>2</sub> particles, respectively. As shown in Figure 10a, a plenty of Pt particles  
261 were evenly deposited on the surface of FeOOH, indicating that the abundant  
262 reduction active sites were uniformly distributed on FeOOH. Besides, it was  
263 interesting to note that the RuO<sub>2</sub> particles were mainly concentrated at the top  
264 edges of X-structures, while the facets showed nearly smooth surfaces (Figure  
265 10b). The selective deposition of RuO<sub>2</sub> implied that the oxidation active sites  
266 were mainly distributed on the edges. It could be induced that under irradiation,

267 the photo-generated electrons would efficiently and evenly transfer to the  
268 surface of X-structured FeOOH crystals, while the holes prefer to migrate to the  
269 edges. Therefore, the efficient electron transfer and charge carrier separation  
270 were realized, which eventually favored the POWS performance of X-structured  
271 FeOOH.

272 It is known that the ratio of exposed facets has a significant influence on the  
273 photocatalytic activity.<sup>[25]</sup> A comparison study of the POWS performance  
274 between FeOOH-LR and FeOOH-120F was conducted. As shown in Figure  
275 S5a and S5b, the FeOOH-LR and FeOOH-120F showed similar particle sizes  
276 of 3.9 and 3.6  $\mu\text{m}$  in length, respectively. However, the branches of FeOOH-LR  
277 were much shorter, leading to a lower ratio of exposed high-index  $\{3\bar{1}\bar{1}\}$   
278 facets. The morphological structures of FeOOH-LR and FeOOH-120F were  
279 illustrated in Figure S5c and S5d. It could be calculated that the ratios of  
280 exposed  $\{3\bar{1}\bar{1}\}$  facets of FeOOH-LR and FeOOH-120F were about 77% and  
281 96%, respectively. It is not surprising that the POWS efficiency of FeOOH-120F  
282 is higher than that of FeOOH-LR (Figure S6), because the exposed  $\{3\bar{1}\bar{1}\}$   
283 facets provide a plenty of well-separated reduction and oxidation active sites,  
284 which is crucial for the POWS activity, as discussed earlier.

285 The cycling tests for the VLD photocatalytic activities of X-structured  $\alpha$ -  
286 FeOOH photocatalyst were conducted to investigate its stability and reusability.  
287 As illustrated in Figure 11, no noticeable decrease was detected in the  $\text{H}_2$  and  
288  $\text{O}_2$  evolution rate after five consecutive cycles (60 h in total) without recovery of  
289 photocatalyst, revealing the excellent photo-stabilization and reusability of the  
290 X-structured  $\alpha$ -FeOOH. Figure S7 showed the XPS spectrum and XRD pattern  
291 of FeOOH-30F after the POWS reaction. The results indicated that the Fe  
292 chemical state, phase and structure of  $\alpha$ -FeOOH remained intact, further  
293 suggesting that the  $\alpha$ -FeOOH photocatalyst was stable in the POWS process.  
294 Therefore, the X-structured  $\alpha$ -FeOOH samples could serve as cost-effective  
295 and highly stable photocatalysts for VLD overall water splitting.

## 296 **Conclusions**

297 In summary, an efficient and stable photocatalyst  $\alpha$ -FeOOH with uniform X-  
298 shaped morphology and multiple high-index facets has been successfully  
299 synthesized through a simple hydrothermal method for the POWS application.  
300 The effects of various physico-chemical parameters on the formation of X-  
301 structured  $\alpha$ -FeOOH were investigated. Efficient POWS was achieved by this  
302 newly prepared photocatalyst, with the maximum  $\text{H}_2$  and  $\text{O}_2$  generation rate  
303 around 9.2 and 4.7  $\mu\text{mol}\cdot\text{h}^{-1}\cdot\text{g}^{-1}$  from pure water under VL irradiation. The good  
304 POWS performance of X-structured  $\alpha$ -FeOOH photocatalyst was ascribed to  
305 the large surface area, high-ratio exposure of high-index facets, high electron  
306 transfer and effective charge separation. The recycling experiments indicated  
307 the excellent stability of X-structured  $\alpha$ -FeOOH photocatalyst. This work  
308 provided an alternative approach of designing a cost-effective, stable, size  
309 controllable, co-catalyst free and VLD photocatalyst for solar-to-fuel  
310 conversion.

## 311 **Experimental section**

### 312 **Materials preparation**

313 Typically,  $\text{FeCl}_2$  (60 mmol),  $\text{FeCl}_3\cdot 6\text{H}_2\text{O}$  (60 mmol), urea (300 mmol) and  $\text{NH}_4\text{F}$   
314 (30 mmol) were dissolved in deionized water (70 mL) by vigorous stirring.  
315 Subsequently, the mixed solution was transferred to a 100-mL Teflon-lined  
316 stainless-steel autoclave, hydrothermally heated at 120 °C for 12 h in a forced  
317 air oven (DNG-9036A, Shanghai Jinghong Manufacturing Company, China),  
318 and then allowed to cool to room temperature. After that, the slurry was mixed  
319 with 200 mL of ethanol (95%) under ultrasonication, and purified by a magnet  
320 several times to completely remove the magnetic impurities. The resulting  
321 yellowish-brown products were obtained by filtrating with a membrane filter (0.2  
322  $\mu\text{m}$ , Millipore), washing several times with deionized water and ethanol, and  
323 finally drying at 60 °C for 12 h. To test the effect of  $\text{NH}_4\text{F}$  content on the  
324 morphology of products,  $\text{NH}_4\text{F}$  concentration-dependent experiments were

325 conducted by using different initial concentrations of  $\text{NH}_4\text{F}$  (i.e. 30, 60, 120 and  
326 180 mmol), the products were accordingly denoted as FeOOH-30F, FeOOH-  
327 60F, FeOOH-120F and FeOOH-180F. For comparison, the plate-like  $\alpha$ -FeOOH  
328 structures were prepared according to a previously reported method.<sup>[26]</sup> In brief,  
329 5 mmol of  $\text{FeSO}_4 \cdot 7\text{H}_2\text{O}$  and 10 mmol of  $\text{CH}_3\text{COONa}$  were dissolved in 50 mL  
330 of deionized water and then vigorously stirred at 40 °C for 6 h. The slurry was  
331 centrifuged and thoroughly washed with deionized water and ethanol, and  
332 finally dried at 60 °C for 12 h. The product was denoted as plate-like FeOOH.  
333 Moreover, to better understand the effect of the ratio of exposed high-index  
334 facets on the photocatalytic activity, the FeOOH with low-ratio exposure of high-  
335 index facets was prepared. The synthesis procedure was similar as that of  
336 FeOOH-120F, expect that the concentration of urea was decreased to 200  
337 mmol and the reaction temperature was decreased to 110 °C. The product was  
338 denoted as FeOOH-LR. All the chemicals used in the experiments were of  
339 reagent grade and used as received without further purification.

#### 340 **Characterization**

341 The morphology of samples was investigated using a Quanta 400F field-  
342 emission scanning electron microscope (FESEM) (FEI Company, USA) and a  
343 Tecnai F20 high-resolution transmission electron microscope (HRTEM, FEI  
344 Company, USA). UV-vis diffuse reflectance spectrum (UV-vis DRS) was  
345 recorded using a Varian Cary 100 UV-vis spectrophotometer (Agilent  
346 Technologies Inc., USA) equipped with a labsphere diffuse reflectance  
347 accessory. The X-ray diffraction (XRD) patterns were obtained on a SmartLab  
348 X-ray diffractometer (Rigaku Corporation, Japan) operating at 40 mA and 40 kV  
349 with  $\text{Cu K}\alpha$  radiation. X-ray photoelectron spectroscopy (XPS) measurements  
350 were performed by a Thermo Scientific ESCALAB 250XI X-ray photoelectron  
351 spectrometer (Thermo Scientific, USA). The specific surface areas and pore-  
352 size distributions were determined using a Quadrasorb-SI Surface Area and  
353 Pore Size Analyzer (Quantachrome Instruments, USA). Room-temperature  
354 photoluminescence (PL) spectra were recorded by an FP-6500 fluorescence

355 spectrometer (Jasco Corporation, Japan), with the excited wavelength ( $\lambda_{ex}$ ) of  
356 365 nm.

### 357 **Photo-depositions of Pt and RuO<sub>2</sub> on X-structured FeOOH**

358 The photo-depositions of Pt and RuO<sub>2</sub> were conducted using H<sub>2</sub>PtCl<sub>6</sub> and RuCl<sub>3</sub>  
359 as metal precursors, respectively. In a typical procedure, 5 mg of FeOOH-30F  
360 and a calculated amount of H<sub>2</sub>PtCl<sub>6</sub> (10 wt%) or RuCl<sub>3</sub>·xH<sub>2</sub>O (10 wt%) were  
361 dispersed in 20 mL of methanol (20 %) or NaIO<sub>3</sub> (0.02 M) solution, respectively.  
362 Then, the suspension was illuminated by a 300W Xeon lamp ( $\lambda \geq 420$  nm) for 1  
363 h under continuous stirring. The products were filtrated, washed thoroughly with  
364 deionized water and ethanol, and dried at 60 °C for 12 h.

### 365 **Photoelectrochemical measurements**

366 The transient photocurrent responses and electrochemical impedance  
367 spectroscopy (EIS) Nyquist plots were obtained from an electrochemical  
368 workstation (CHI 660D, Shanghai Chenhua Instrument Company, China) in a  
369 three-electrode quartz cell with Na<sub>2</sub>SO<sub>4</sub> (0.1 M) electrolyte solution. Ag/AgCl  
370 and Pt were used as the reference and the counter electrodes, respectively.  
371 Typically, 5 mg of the as-prepared photocatalyst and 10  $\mu$ L of Nafion<sup>®</sup> 117  
372 solution (5 wt%) were well dispersed in a 0.5 mL water/isopropanol mixed  
373 solvent (3:1 v/v) by sonication to form a homogeneous colloid. Subsequently,  
374 100  $\mu$ L of the colloid was deposited on a fluorinated-tin-oxide (FTO) glass with  
375 an area of 1 cm<sup>2</sup> and dried in air at room temperature. The electrodes were held  
376 at the potential of +0.6 V. A 300W Xeon lamp was used as the light source in  
377 the photocurrent measurement.

### 378 **Photocatalytic reactions**

379 Photocatalytic reactions were conducted at approximately 25°C in a Labsolar-  
380 IIIAC closed gas circulation system (Beijing Perfect Light Technology Co., Ltd  
381 China). Typically, 100 mg of photocatalyst was dispersed by a magnetic stirrer  
382 into 100 mL of pure water in a 400-mL Pyrex reactor. Prior to irradiation, the  
383 suspension was evacuated several times to completely remove air.  
384 Subsequently, the suspension was irradiated using a 300W Xeon lamp (PLS-

385 SXE300C, Beijing Perfect Light Technology Co., Ltd China) with a 420-nm UV  
386 cut-off filter. At given time intervals, the evolved gases were analyzed by an  
387 online GC-7990II gas chromatograph (Zhejiang Fuli Analytical Instrument Co.,  
388 Ltd., China) equipped with a 5 Å molecular sieve column and a thermal  
389 conductivity detector (TCD). Argon was used as the carrier gas.

## 390 Acknowledgements

391 This research was financially supported by the research grant  
392 (GRF14100115) from Research Grant Council and ITSP Tier 3 Scheme  
393 (ITS/216/14) from Innovation and Technology Commission of Hong Kong SAR  
394 Government. H.J. Zhao and P.K. Wong were also supported by the CAS/SAFEA  
395 International Partnership Program for Creative Research Teams (2015HSC-  
396 UE004) of Chinese Academy of Sciences, China. Z.F. Jiang was supported by  
397 the National Natural Science Foundation of China (21706102), Natural Science  
398 Foundation of Jiangsu Province (BK20170527) and Hong Kong Scholar  
399 Program (XJ2016034), China. The authors would also like to acknowledge the  
400 technical supports from Prof. Jimmy Yu Laboratory and Tianhe Scientific  
401 Collaboration Center, China.

402 **KEYWORDS:** iron oxyhydroxide • X-like structure • high-index facet • charge  
403 separation • water splitting

404

## 405 References

- 406 [1] R. M. Navarro Yerga, M. C. Álvarez Galván, F. Del Valle, J. A. Villoria de la Mano, J. L.  
407 Fierro, *ChemSusChem* **2009**, *2*, 471–485.
- 408 [2] a) M. C. Hsieh, G. C. Wu, W. G. Liu, W. A. Goddard, C. M. Yang, *Angew. Chem. Int.*  
409 *Edit.* **2014**, *53*, 14216–14220; b) X. J. Lv, S. X. Zhou, X. Huang, C. J. Wang, W. F. Fu,  
410 *Appl. Catal. B: Environ.* **2016**, *182*, 220–228; c) K. Y. Yoon, H. J. Ahn, M. J. Kwak, S. I.  
411 Kim, J. Park, J. H. Jang, *J. Mater. Chem. A.* **2016**, *4*, 18730–18736.
- 412 [3] a) H. Fujito, H. Kunioku, D. Kato, H. Suzuki, M. Higashi, H. Kageyama, R. Abe, *J. Am.*  
413 *Chem. Soc.* **2016**, *138*, 2082–2085; b) L. Ye, K. H. Chu, B. Wang, D. Wu, H. Xie, G.  
414 Huang, H. Y. Yip, P. K. Wong, *Chem. Commun.* **2016**, *52*, 11657–11660.
- 415 [4] M. Hadnadjev-Kostic, T. Vulic, J. Ranogajec, R. Marinkovic-Neducin, A. Radosavljevic-  
416 Mihajlovic, *J. Therm. Anal. Calorim.* **2013**, *111*, 1155–1162.

- 417 [5] a) Y. Negishi, Y. Matsuura, R. Tomizawa, W. Kurashige, Y. Niihori, T. Takayama, A.  
418 lwase, A. Kudo, *J. Phys. Chem. C* **2015**, *119*, 11224–11232; b) J. Ran, J. Zhang, J. Yu,  
419 M. Jaroniec, S. Z. Qiao, *Chem. Soc. Rev.* **2014**, *43*, 7787–7812; c) T. M. Breault, J. J.  
420 Brancho, P. Guo, B. M. Bartlett, *Inorg. Chem.* **2013**, *52*, 9363–9368; d) S. Cao, C. J.  
421 Wang, W. F. Fu, Y. Chen, *ChemSusChem* **2017**, *10*, 4306–4323.
- 422 [6] a) W. D. Chemelewski, H.-C. Lee, J.-F. Lin, A. J. Bard, C. B. Mullins, *J. Am. Chem. Soc.*  
423 **2014**, *136*, 2843–2850; b) Y. Zheng, Z. Zhang, C. Li, *J. Mol. Catal. A: Chem.* **2016**, *423*,  
424 463–471; c) D. K. Padhi, K. Parida, *J. Mater. Chem. A* **2014**, *2*, 10300–10312; d) M.  
425 C. Pereira, E. M. Garcia, A. C. da Silva, E. Lorençon, J. D. Ardisson, E. Murad, J. D.  
426 Fabris, T. Matencio, T. de Castro Ramalho, M. V. J. Rocha, *J. Mater. Chem.* **2011**, *21*,  
427 10280–10282.
- 428 [7] J. A. Seabold, K. S. Choi, *J. Am. Chem. Soc.* **2012**, *134*, 2186–2192.
- 429 [8] J. Y. Kim, D. H. Youn, K. Kang, J. S. Lee, *Angew. Chem. Int. Edit.* **2016**, *55*, 10854–  
430 10858.
- 431 [9] T. da Silva Rocha, E. S. Nascimento, A. C. da Silva, H. dos Santos Oliveira, E. M.  
432 Garcia, L. C. A. de Oliveira, D. S. Monteiro, M. Rodriguez, M. C. Pereira, *RSC Adv.*  
433 **2013**, *3*, 20308–20314.
- 434 [10] a) H. Li, W. Li, Y. Zhang, T. Wang, B. Wang, W. Xu, L. Jiang, W. Song, C. Shu, C. Wang,  
435 *J. Mater. Chem.* **2011**, *21*, 7878–7881; b) Y. Zhang, P. Yan, Q. Wan, K. Wu, N. Yang,  
436 *Electrochem. Commun.* **2016**, *68*, 10–14; c) C. Zhang, J. Zhu, X. Rui, J. Chen, D. Sim,  
437 W. Shi, H. H. Hng, T. M. Lim, Q. Yan, *CrystEngComm* **2012**, *14*, 147–153.
- 438 [11] X. Zhou, H. Yang, C. Wang, X. Mao, Y. Wang, Y. Yang, G. Liu, *J. Phys. Chem. C* **2010**,  
439 *114*, 17051–17061.
- 440 [12] S. Kakuta, T. Numata, T. Okayama, *Catal. Sci. & Technol.* **2014**, *4*, 164–169.
- 441 [13] N. Tian, Z.-Y. Zhou, S.-G. Sun, Y. Ding, Z. L. Wang, *Sci.* **2007**, *316*, 732–735.
- 442 [14] Y. Liu, H. Liu, Q. Zhang, T. Li, *RSC Adv.* **2017**, *7*, 3515–3520.
- 443 [15] M. Leng, M. Z. Liu, Y. B. Zhang, Z. Q. Wang, C. Yu, X. G. Yang, H. J. Zhang, C. Wang,  
444 *J. Am. Chem. Soc.* **2010**, *132*, 17084–17087.
- 445 [16] R. M. Cornell, U. Schwertmann, *The iron oxides: structure, properties, reactions,*  
446 *occurrences and uses*, John Wiley & Sons, **2003**, p 71.
- 447 [17] a) Z. Jiang, K. Qian, C. Zhu, H. Sun, W. Wan, J. Xie, H. Li, P. K. Wong, S. Yuan, *Appl.*  
448 *Catal. B: Environ.* **2017**, *210*, 194–204; b) P. Kie, P. Persson, L. Osterlund, *J. Phys.*  
449 *Chem. C* **2012**, *116*, 14917–14929.
- 450 [18] M. Hojamberdiev, G. Zhu, A. Eminov, K. Okada, *J. Cluster Sci.* **2013**, *24*, 97–106.
- 451 [19] K. H. Chu, L. Ye, W. Wang, D. Wu, D. K. L. Chan, C. Zeng, H. Y. Yip, C. Y. Jimmy, P. K.  
452 Wong, *Chemosphere* **2017**, *183*, 219–228.
- 453 [20] a) T. Yamashita, P. Hayes, *Appl. Surf. Sci.* **2008**, *254*, 2441–2449; b) C. Long, L. Jiang,  
454 T. Wei, J. Yan, Z. Fan, *J. Mater. Chem. A* **2014**, *2*, 16678–16686; c) M. C. Biesinger,  
455 B. P. Payne, A. P. Grosvenor, L. W. Lau, A. R. Gerson, R. S. C. Smart, *Appl. Surf. Sci.*  
456 **2011**, *257*, 2717–2730.
- 457 [21] a) J. Q. Liu, M. B. Zheng, X. Q. Shi, H. B. Zeng, H. Xia, *Adv. Funct. Mater.* **2016**, *26*,  
458 919–930; b) Y.-X. Zhang, Y. Jia, *Appl. Surf. Sci.* **2014**, *290*, 102–106; c) Q. Yu, X. Meng,  
459 T. Wang, P. Li, J. Ye, *Adv. Funct. Mater.* **2015**, *25*, 2686–2692.
- 460 [22] Y. Wang, L. Zhu, N. Ba, F. Gao, H. Xie, *Mater. Res. Bull.* **2017**, *86*, 268–276.

- 461 [23] Y. Xie, *Adv. Funct. Mater.* **2006**, *16*, 1823–1831.
- 462 [24] a) Z. Jiang, W. Wan, W. Wei, K. Chen, H. Li, P. K. Wong, J. Xie, *Appl. Catal. B: Environ.*  
463 **2017**, *204*, 283-295; b) H. Li, Y. Liu, X. Gao, C. Fu, X. Wang, *ChemSusChem* **2015**, *8*,  
464 1189–1196.
- 465 [25] C. Liu, X. Han, S. Xie, Q. Kuang, X. Wang, M. Jin, Z. Xie, L. Zheng, *Chem. Asian J.*  
466 **2013**, *8*, 282–289.
- 467 [26] Q. Hao, S. Liu, X. Yin, Y. Wang, Q. Li, T. Wang, *Solid State Sci.* **2010**, *12*, 2125–2129.

468  
469  
470  
471  
472  
473  
474  
475  
476  
477  
478  
479  
480  
481  
482  
483  
484  
485  
486  
487  
488  
489  
490  
491  
492  
493  
494  
495  
496  
497  
498  
499  
500  
501  
502  
503  
504

## Tables and Figures

505

506

507

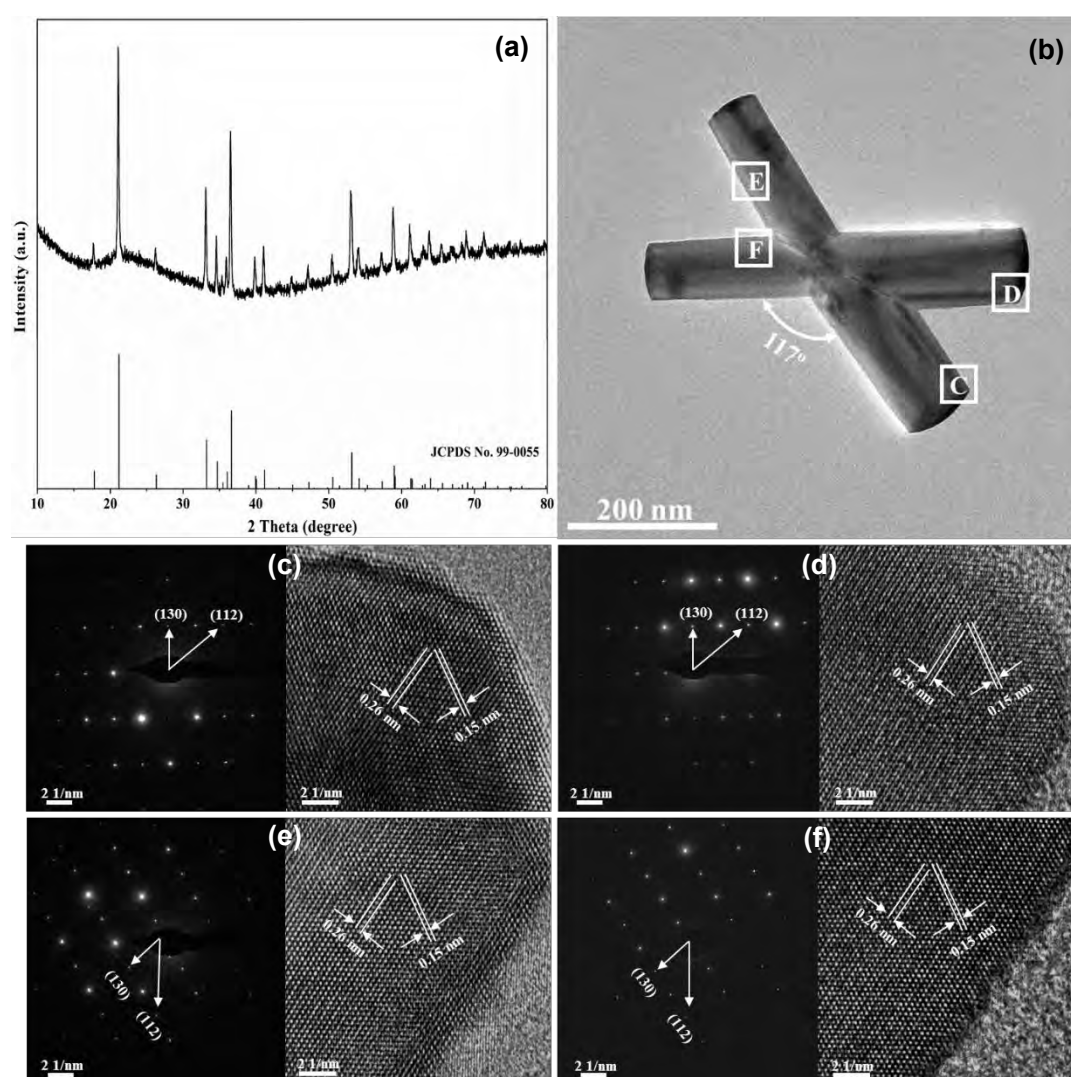
508

Table 1. The average particle sizes, specific surface areas, pore volumes and pore sizes of the as-synthesized samples

Sample	Length ( $\mu\text{m}$ )	Width ( $\mu\text{m}$ )	Surface area ( $\text{m}^2\text{g}^{-1}$ )	Pore volume ( $\text{cm}^3\text{g}^{-1}$ )	Pore size (nm)
FeOOH-30F	0.60	0.35	29.60	0.10	2.37
FeOOH-60F	1.10	0.56	19.51	0.05	1.32
FeOOH-120F	3.60	1.82	11.30	0.03	1.32
FeOOH-180F	5.85	3.20	19.07	0.05	1.32
Plate-like FeOOH	0.43	0.35	40.19	0.09	4.08

509

510



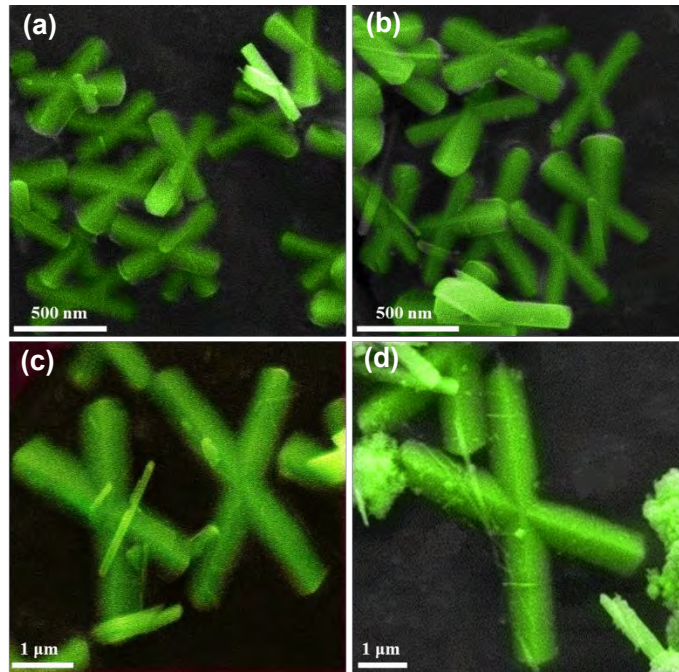
511

Figure 1. (a) XRD pattern, (b) TEM image and (c)-(f) SAED patterns (left) and HRTEM

images (right) of FeOOH-30F (SAED and HRTEM were accordingly obtained from the

positions labeled in Figure 1b)

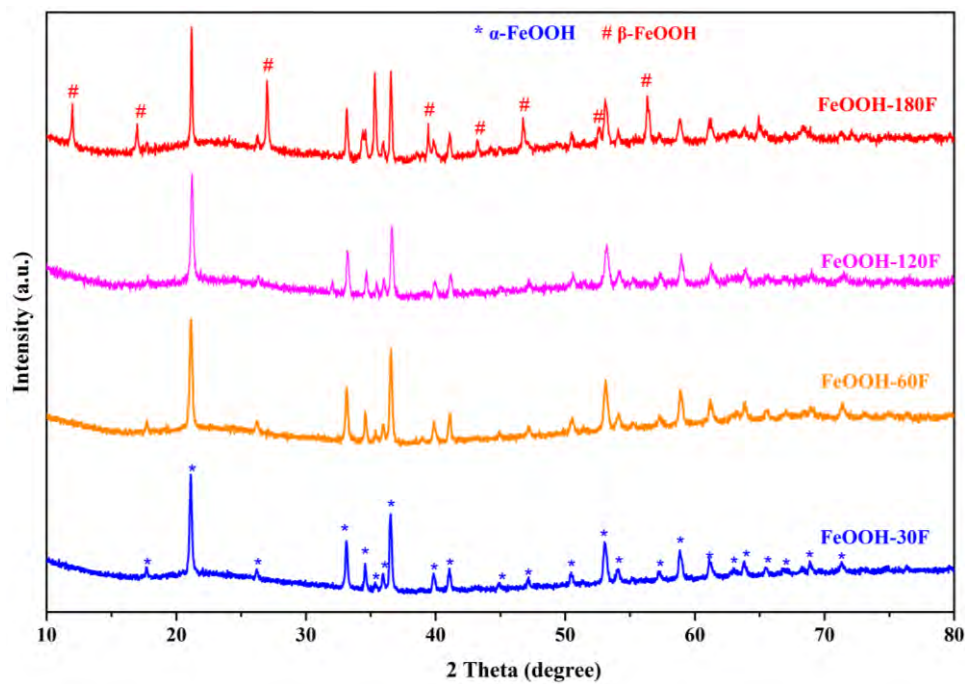
515



516

517 Figure 2. FESEM images of (a) FeOOH-30F, (b) FeOOH-60F (c) FeOOH-120F and (d)  
518 FeOOH-180F

519



520

521 Figure 3. XRD patterns of FeOOH-30F, FeOOH-60F, FeOOH-120F and FeOOH-180F

522

523

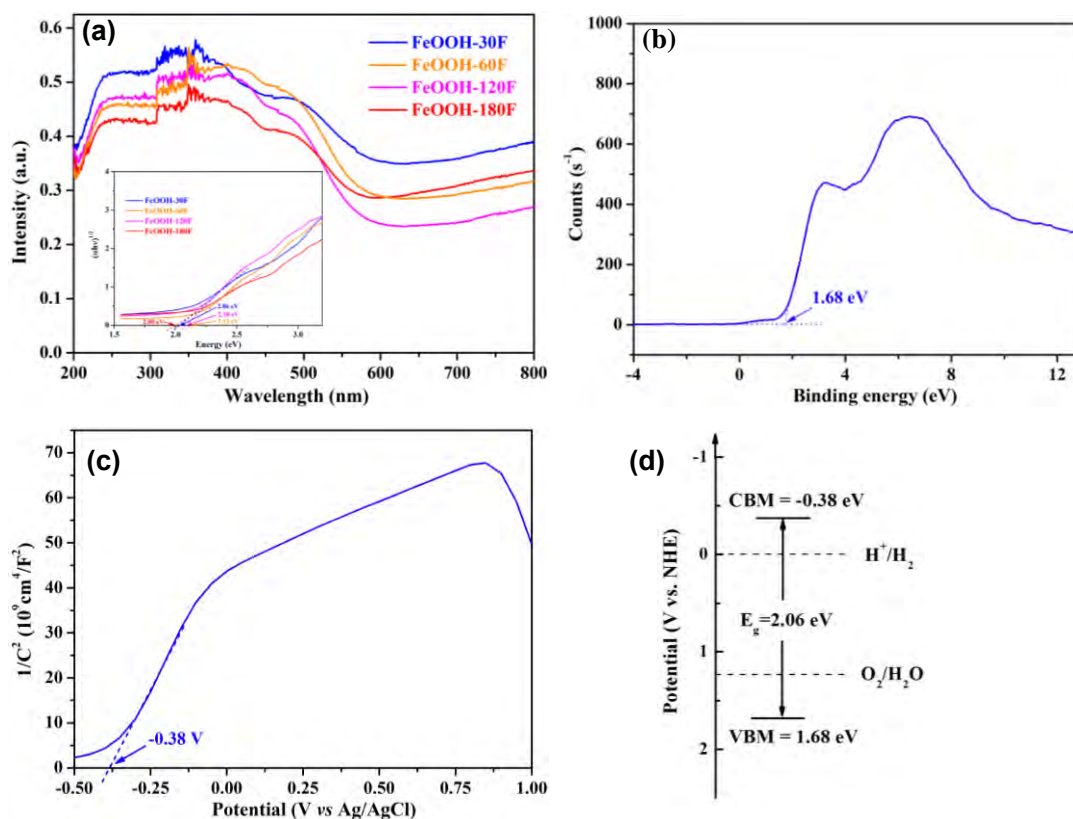
524

525

526

527

528

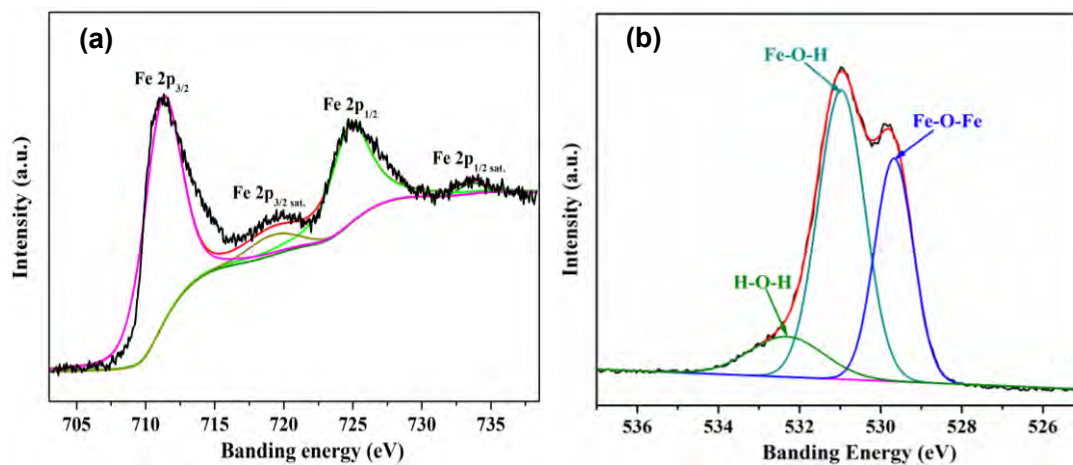


529

530

531 Figure 4. (a) UV-vis DRS patterns of X-structured FeOOH photocatalysts (inset shows the  
 532 plots of transformed Kubelka–Munk function versus light energy), (b) valance band XPS  
 533 spectrum, (c) Mott-Schottky plot and (d) band structure of FeOOH-30F

534

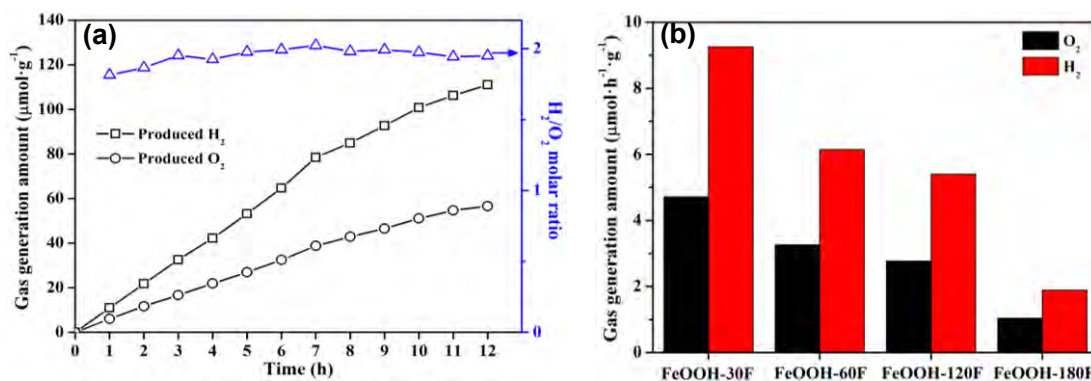


535

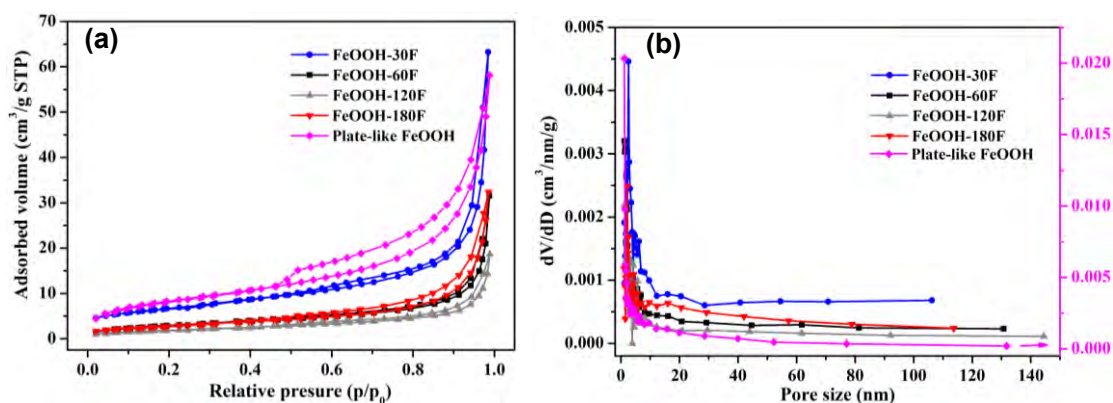
536 Figure 5. XPS spectra of (a) Fe 2p and (b) O 1s of FeOOH-30F

537

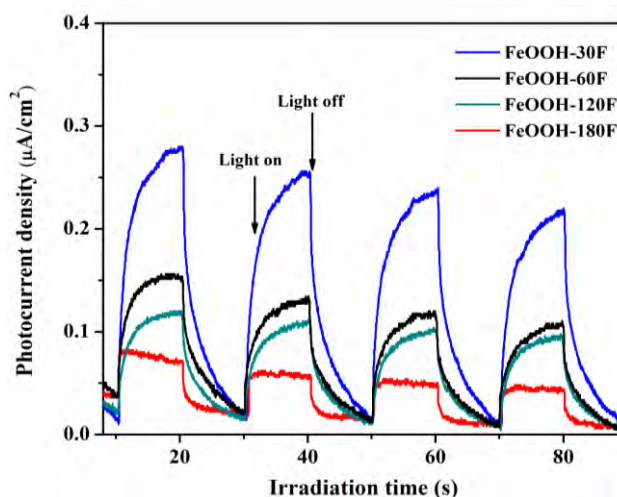
538



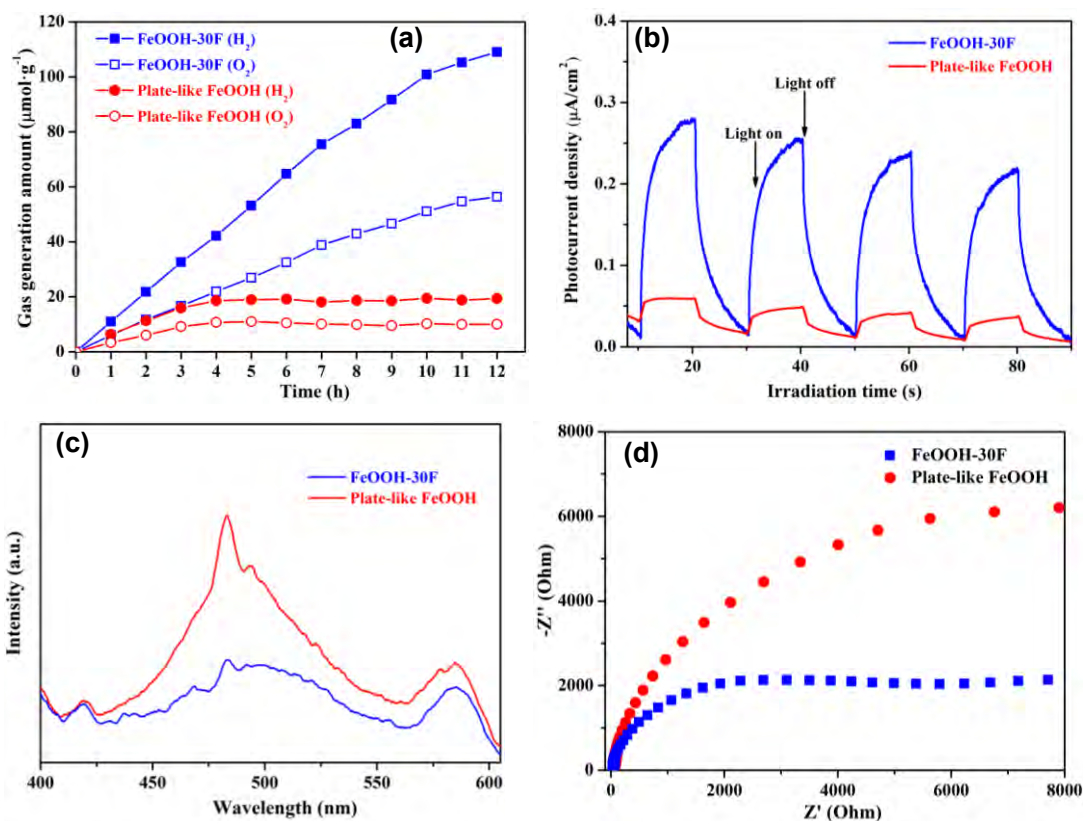
539  
 540 Figure 6. (a) Time courses of photocatalytic H<sub>2</sub> and O<sub>2</sub> evolution from pure water over  
 541 FeOOH-30F under VL irradiation and (b) photocatalytic H<sub>2</sub> and O<sub>2</sub> generation amounts over  
 542 different FeOOH photocatalysts under VL irradiation  
 543  
 544



545  
 546 Figure 7. (a) N<sub>2</sub> adsorption-desorption isotherms and (b) pore size distributions of the as-  
 547 prepared samples.  
 548  
 549



550  
 551 Figure 8. Transient photocurrent responses of FeOOH samples (condition: potential =  
 552 +0.6V; reference electrode: Ag/AgCl; counter electrode: Pt; electrolyte solution: Na<sub>2</sub>SO<sub>4</sub>,  
 553 0.1M)  
 554

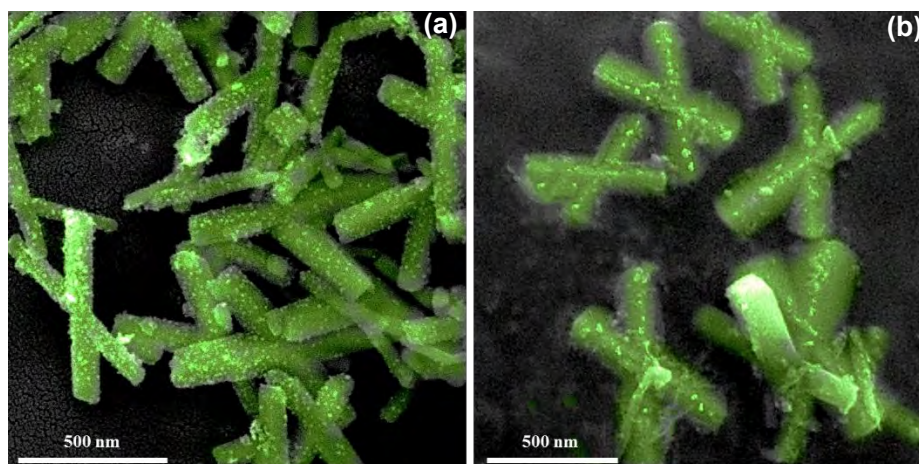


555

556

557 Figure 9. (a) Photocatalytic  $\text{H}_2$  and  $\text{O}_2$  evolution from pure water over FeOOH-30F and  
 558 plate-like FeOOH under VL irradiation, (b) transient photocurrent responses (the condition  
 559 is the same as that shown in Figure 8), (c) room-temperature photoluminescence spectra  
 560 ( $\lambda_{\text{ex}} = 365 \text{ nm}$ ) and (d) EIS Nyquist plots of FeOOH-30F and plate-like FeOOH

561



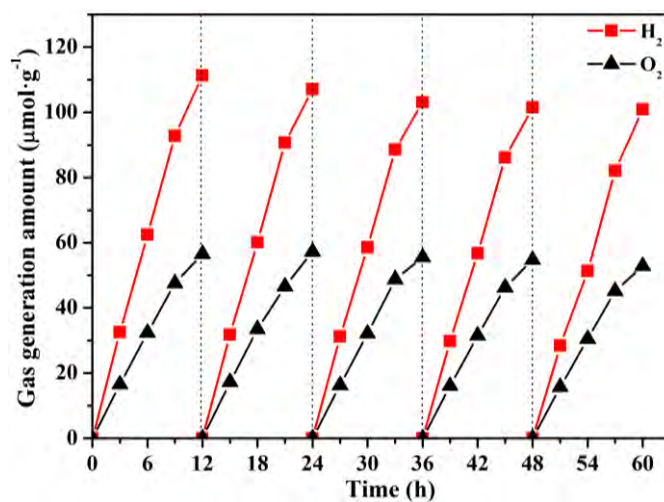
562

563 Figure 10. FESEM images of FeOOH-30F after the photo-depositions of (a) Pt and (b)  
 564  $\text{RuO}_2$

565

566

567



568

569

570

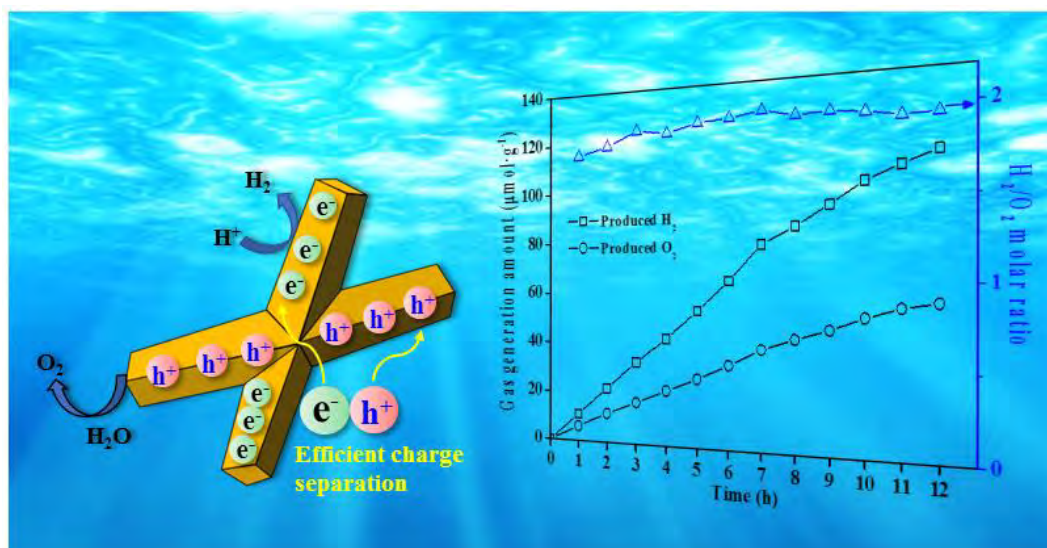
571

Figure 11. Time courses of H<sub>2</sub> and O<sub>2</sub> evolution from pure water over FeOOH-30F under VL irradiation

572 **Graphical Abstract**

573

574 An X-structured  $\alpha$ -FeOOH photocatalyst with multiple high-index facets and enhanced  
575 charge separation was fabricated and used for photocatalytic overall water splitting under  
576 visible light irradiation



577